

Sentinel-1 and Sentinel-2 Spatio-Temporal Data Fusion for Clouds Removal

Alessandro Sebastianelli , Artur Nowakowski, Erika Puglisi, Maria Pia Del Rosso , Jamila Mifdal, Fiora Pirri, Pierre Philippe Mathieu, Silvia Liberata Ullo 

Abstract—The abundance of clouds, located both spatially and temporally, often makes remote sensing applications with optical images difficult or even impossible. In this manuscript a novel method for clouds-corrupted optical images restoration has been presented and developed, based on a joint data fusion paradigm, where three deep neural networks have been combined in order to fuse spatio-temporal features extracted from Sentinel-1 and Sentinel-2 time-series of data. It is worth to highlight that both the code and the dataset have been implemented from scratch and made available to interested research for further analysis and investigation.

Index Terms—Data Fusion, Clouds removal, Sentinel-1, Sentinel-2, Deep Learning, Convolutional Neural Networks (CNNs).

I. INTRODUCTION

REMOTE sensing applications with optical images, are hindered by cloud masses. The abundance of clouds, located both spatially and temporally, often makes remote sensing applications with optical images difficult or even impossible. For example the four global cloud maps of 2020 in Figure 1, show that there are only a few places on the globe that are not significantly covered by clouds. In other words in some places the clouds can cover the Area of Interest (AOI) for several months in a row.

Traditional clouds removing techniques has been subject of studies since decades, but recently also Machine Learning (ML) approaches have been developed to tackle this field of Remote Sensing (RS).

Traditional approaches can be categorized in three main groups: 1) Multi-Spectral, 2) Multi-Temporal and 3) In-Painting. Multi-Spectral approaches can be applied when the optical signal are only partially affected by clouds, because this kind of techniques exploit weak signals to restore surface information without the used of additional data. The methodologies used can be mathematical [2], [3], physical [4]–[7] or geometry-based [8]. Multi-Temporal approaches can restore cloudy scenes by integrating information from previous acquisitions with cloud-free conditions [9] [10], [11]. In some studies the integrated information can be also of different

nature, like in [12], where the cloud-free reference image is obtained by the fusion of two or more low-resolution images coming from different sensors. In-Painting approaches can use cloud-detection algorithms to detect the cloudy part of an image so as to reconstruct it using the other clear parts [13], [14].

In parallel to this traditional approaches, the advent of the Big Data era in Satellite Remote Sensing opens new possibilities for the resolution of the problem using powerful data-driven deep learning methods.

The first paper exploiting the potential of Deep Convolutional Neural Networks for restoring missing information in remote sensing imagery was [15] that uses a Spatial–Temporal–Spectral (STS) Convolutional Neural Network to restore data gaps using multi-source data. However, STS cannot effectively reconstruct large-scale areas and can only utilize single temporal images, this is why in [16] the same authors improved their model enabling the possibility to use an arbitrary numbers of temporal images to remove cloud and cloud shadow.

Other studies are, instead, focused on the potential of Generative Adversarial Networks (GANs) [17], [18] that can be used as a solution to the problem or as an auxiliary instrument (e.g. Mirza and Osindero in [19] introduced the conditional-GANs which are able to generate fake images similar to real images). For example, in [20] is presented the first conditional GAN (cGAN) able to fuse SAR and optical multi-spectral images with the intent of generating cloud/haze-free optical data from images corrupted by clouds. A similar approach is also proposed by [21] that uses a Deep Residual Neural Network (instead of a GAN) to remove clouds from multi-spectral Sentinel-2 images: also there is used a SAR-optical data fusion method to exploit the synergistic properties of the two imaging systems and guide the reconstruction.

A different kind of GAN is proposed by [22], that, with the intent of capturing correlations across multiple images over an area, presents a Spatio-Temporal Generator Network (STGAN) able to remove clouds using a concatenation between three previous acquisitions of the area of interest. Also [23] proposes a similar approach, but with a different model: firstly the feature informations are extracted from the previous time steps via a special gating function and then a U-net model is used to obtain the desired output image. A particular type of GAN is, instead, proposed by [24] which introduces the spatial attention mechanism into the remote sensing imagery cloud removal task proposing a Spatial Attention GAN (SpA GAN).

The main problem of all these networks is that to be trained

A. Sebastianelli, M. P. Del Rosso and S. L. Ullo are with the Engineering Department, University of Sannio, Benevento, Italy, email: sebastianelli, mariapia.delrosso, ullo@unisannio.it

A. Nowakowski is with Warsaw University of Technology, Warsaw, masovian, Poland, email: artur.nowakowski@pw.edu.pl

E. Puglisi and F. Pirri are with La Sapienza University, Rome, Italy, email: puglisi.1601231@studenti.uniroma1.it, pirri@diag.uniroma1.it

J. Mifdal and P. P. Mathieu are with the European Space Agency, Φ-lab, Frascati, Italy, email: jamila.mifdal, pierre.philippe.mathieu@esa.int

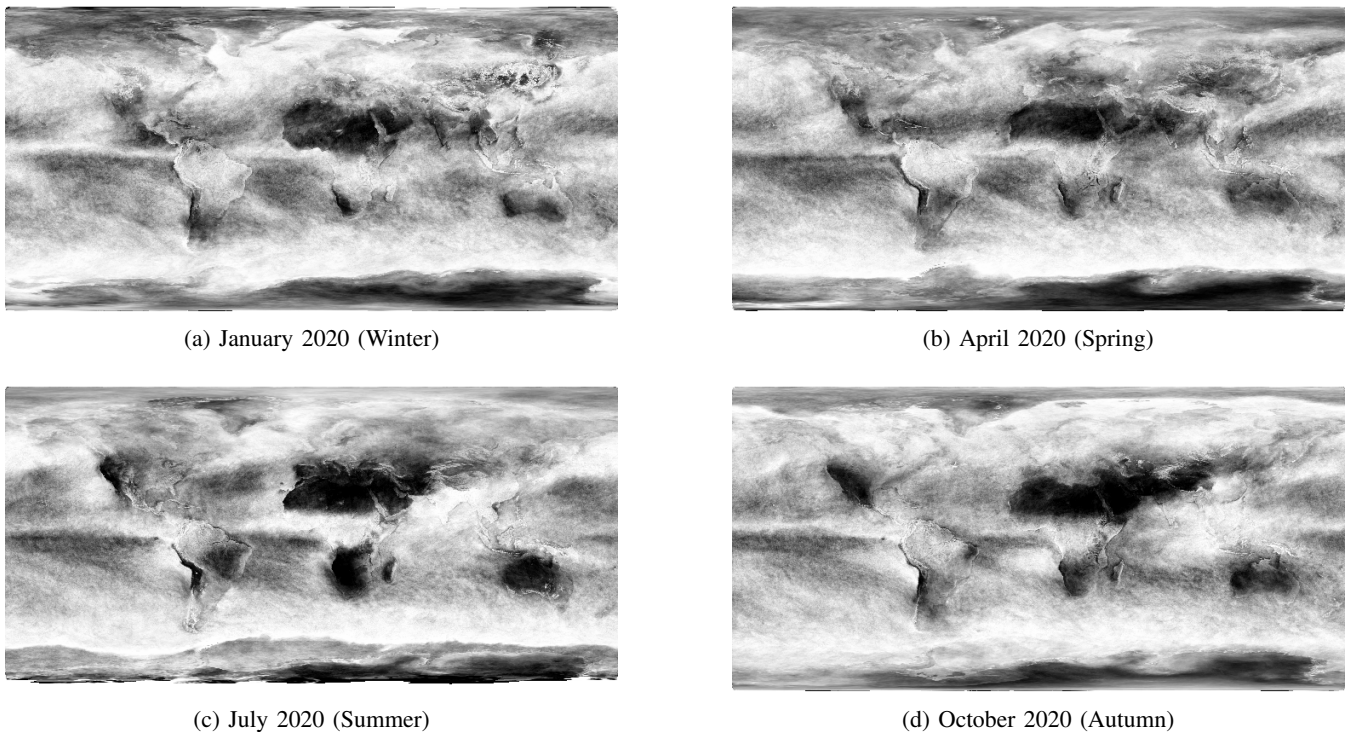


Fig. 1: These maps, made from NASA satellite observations, show how much of Earth’s surface is covered by clouds for a given day, or over a span of days (source [1])

they need paired datasets containing the cloudy images and their cloud-free counterparts. For this reason authors of [25] proposed the Cycle-GAN, that in fact is able to learn the map between cloudy and cloud-free images without the use of a paired dataset or any additional spectral information.

Another different approach studied for generating cloud-free images is to perform a direct translation from SAR to optical: in [26] an optical image is simulated from either a single SAR image or multi-temporal SAR-optical image thanks to a CNN model and a cGAN model. Also in [27] the SAR data is translated into a simulated optical image using a CNN and then a GAN model fuses the SAR data and the simulated and real optical images to reconstruct the missing parts and get a cloud-free output. In [28], instead, two GANs are used: the first one translates SAR images into optical images and the second one removes the clouds using the translated images of the first model.

However, even if different kind of models and approaches exist and despite the powerful generative capabilities that characterize the GANs, these models in particular suffer from training and prediction instabilities that do not allow a simple and reliable use in remote sensing. This is why they are often combined with other types of networks and are rarely used alone.

II. PROPOSED APPROACH

The proposed approach is based on the fusion of the Sentinel-1 SAR (Synthetic Aperture Radar) and Sentinel-2 Multi-spectral data. The method is based on the Joint Data Fusion paradigm [29], as shown in Figure 2, where the multi-spectral (input A) and SAR (input B) data are processed by two

different neural network, then the aggregation of the features extracted by the two neural networks (features A and features B) are used by an another network to estimate the final output.

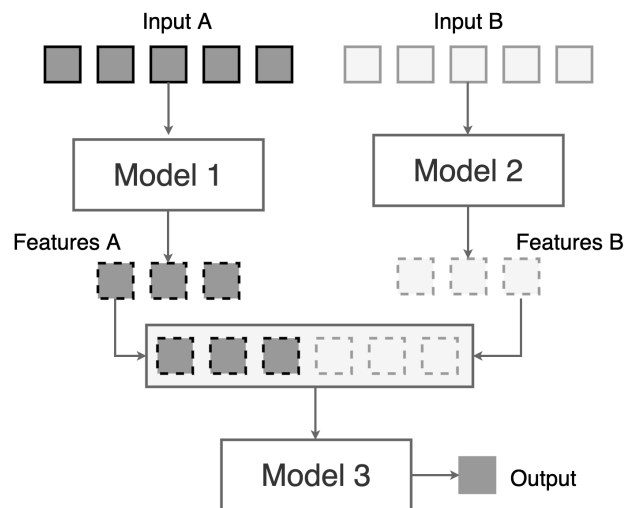


Fig. 2: Joint Data Fusion Paradigm

In our case, "Model 1" is a Convolutional LSTM (Long Short-Term Memory) network, "Model 2" is a pix2pix GAN (Generative Adversarial Network) and Model 3 is a CNN (Convolutional Neural Network) based on the U-Net [30]–[32]. The overall architecture is summarized by the Figure 3, schematized as Figure 2.

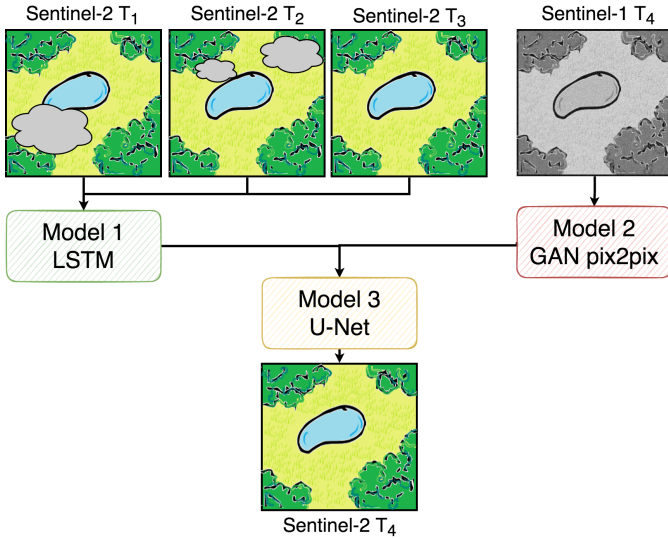


Fig. 3: Proposed architecture

A. LSTM based Optical to Optical translation

The LSTM based model is responsible to the Optical to Optical domain translation, so starting from a set of optical images is able to compute the estimation of a new image in the same domain.

In this case, the optical image is a Sentinel-2 image that can be expressed as a matrix $\mathbf{X}^{\text{S}2} \in \mathbb{R}^{W \times H, B}$, where W and H are respectively the width and the height of the image expressed in number of pixel, while B represents the number of spectral bands (in this paper only RGB bands are involved).

The LSTM based model takes as input a time-series of three Sentinel-2 images $\tilde{\mathbf{X}}^{\text{S}2}_{\text{input}} \in \mathbb{R}^{T \times W \times H, B}$, where T denotes the size of the time-series, and based on the information captured is able to generate the fourth one $\mathbf{Y}^{\text{S}2}_{\text{output}} \in \mathbb{R}^{W \times H, B}$, the image that is virtually covered by clouds.

The proposed architecture is composed of three Convolutional LSTM 2D layers alternated with Max Pooling and Batch Normalisation layers (see Fig. 4). With this configuration the model will perform a blending of the three input images generating a new image.

During the training of the LSTM model, lasting 20 epochs, a batch of 16 Sentinel-2 series $\tilde{\mathbf{X}}^{\text{S}2}_{\text{input}}$ is used as feedforward input for the network. The predicted images $\mathbf{Y}^{\text{S}2}_{\text{output}}$ is compared with the ground truth $\hat{\mathbf{Y}}^{\text{S}2} \in \mathbb{R}^{W \times H \times B}$ through the Mean Absolute Error loss function. Using the loss function and its gradient, the Adam optimiser, with a learning rate of 0.0001, updates the weights of the network.

B. GAN based SAR to Optical translation

The GAN model is used for the SAR to Optical domain translation, and it is responsible of introducing more information, both spatial and temporal. The GAN model is able to produce the fourth optical image $\mathbf{Y}^{\text{S}2}_{\text{output}}$ using as input the corresponding acquisition in the SAR domain $\mathbf{X}^{\text{S}1} \in \mathbb{R}^{W \times H, P}$, where W and H are the same parameters described above and P is the number of different polarization of the SAR acquisition (in this paper only VV polarization has

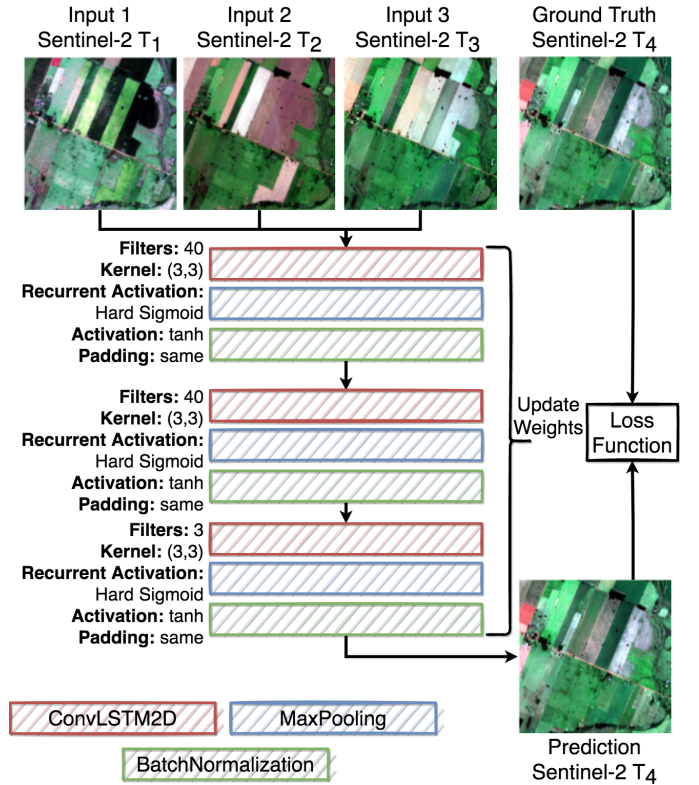


Fig. 4: LSTM model for Optical to Optical translation

been considered). The new temporal and spatial information are introduced by the SAR image that is immune to clouds, and so if a significant temporal (e.g. seasonal evolution) and spatial (e.g. deforestation, new buildings) change in the 4th acquisition is captured by the SAR sensor, the GAN is able to use these information to generate the new optical data.

The proposed GAN architecture, is obviously composed of two sub-networks: the generator and the discriminator, as shown in Fig. 5.

The generator is based upon the U-net, that is essentially an autoencoder with skip connections. The encoder branch is composed of Convolutional 2D layers alternated with Batch Normalisation and LeakyRelu layers. On the other hand, the decoder branch is composed of Convolutional 2D Transpose Layers alternated with Batch Normalisation, Dropout and ReLU layers. Some stages of the encoder branch are then connected with the decoder branch with skip connection.

The discriminator is a pure classifier, it is composed of several Convolutional 2D, Batch Normalisation and LeakyRelu layers.

During the training of the GAN model a batch of 32 Sentinel-1 acquisition $\tilde{\mathbf{X}}^{\text{S}1}$ is used as feedforward input for the generator. The predicted images $\mathbf{Y}^{\text{S}2}_{\text{output}}$ is compared with the ground truth $\hat{\mathbf{Y}}^{\text{S}2}$ through the discriminator and the Mean Squared Error as loss function. Using the loss function and its gradient, the Adam optimiser, with a learning rate of 0.0002, updates the weights of the network.

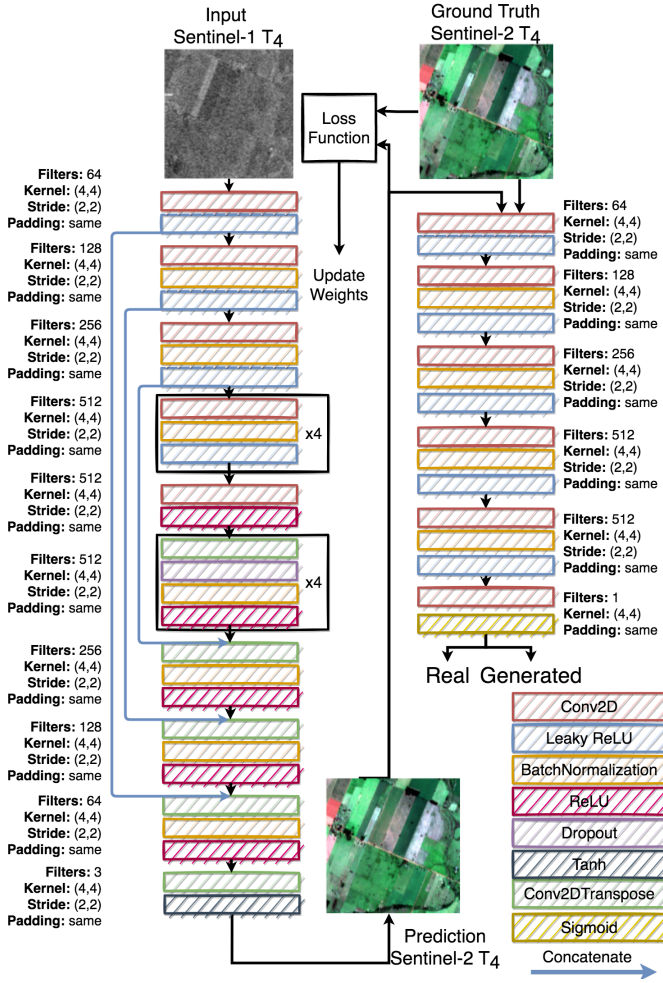


Fig. 5: GAN-Generator model for SAR to optical translation (left branch); GAN-Discriminator model for SAR to optical translation (right branch).

C. Combining Solutions

In order to fuse the LSTM and GAN generated optical images, a model based on the U-Net has been introduced in the overall architecture. The proposed architecture is similar to the GAN generator (see Fig. 6), but in this case the model takes as inputs the LSTM and the GAN outputs.

During the training of the combiner model a batch of 16 couple of LSTM generated images and GAN generated images are used as feedforward input for the model. The predicted images $\hat{Y}^* \in \mathbb{R}^{W \times H \times B}$ is compared with the ground truth \hat{Y} through the Mean Squared Error as loss function. Using the loss function and its gradient, the Adam optimiser, with a learning rate of 0.0001, updates the weights of the network.

III. RESULTS AND EVALUATION METHODS

A. Dataset

The dataset, implemented specifically for the application, contains corresponding Sentinel-1 and Sentinel-2 acquisitions randomly distributed on the Earth surface. For each geographical region there is a time series of four images, acquired with a one month time interval. The aim of this dataset is to power the

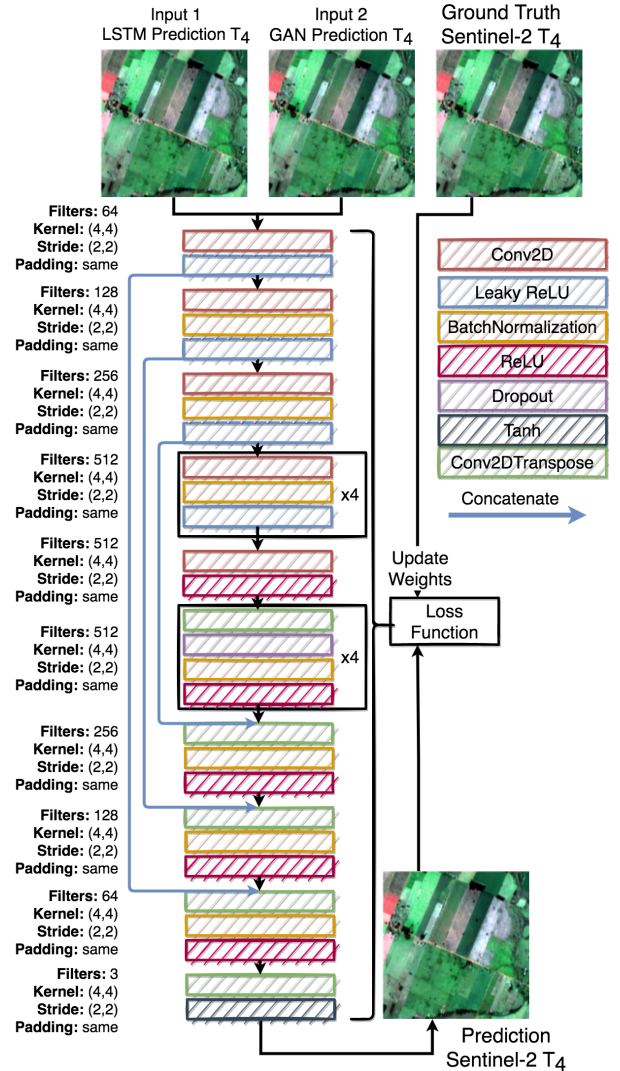


Fig. 6: U-Net based model for the fusion of LSTM and GAN predictions.

exploration of cross modal and temporal AI based applications. The dataset has been built using the *Satellite Data Downloader Tool* proposed in [33].

The dataset contains roughly 8000 Sentinel-1 and 8000 Sentinel-2 images or 2000 Sentinel-1 and 2000 Sentinel-2 time-series of 4 images. Each image has a shape of 256x256 pixels, for Sentinel-1 images there is only the VV polarisation, resulting in a matrix with a shape of 256x256x1; for Sentinel-2 there are the red, green and blue bands, resulting in a matrix with a shape of 256x256x3, and an extra matrix with a shape of 256x256x1 for the cloud mask (QA60 band).

Both Sentinel-1 and Sentinel-2 acquisitions are globally distributed. There are 141 different geographical ROIs (Regions of Interest). Each time-series can correspond to a sequence of 4 months of 2018. An example of time-series taken from the dataset is shown in Fig. 7.

B. Training and validation split

Since the dataset has been created by random acquisition over the globe, it was necessary to develop a strategy for the

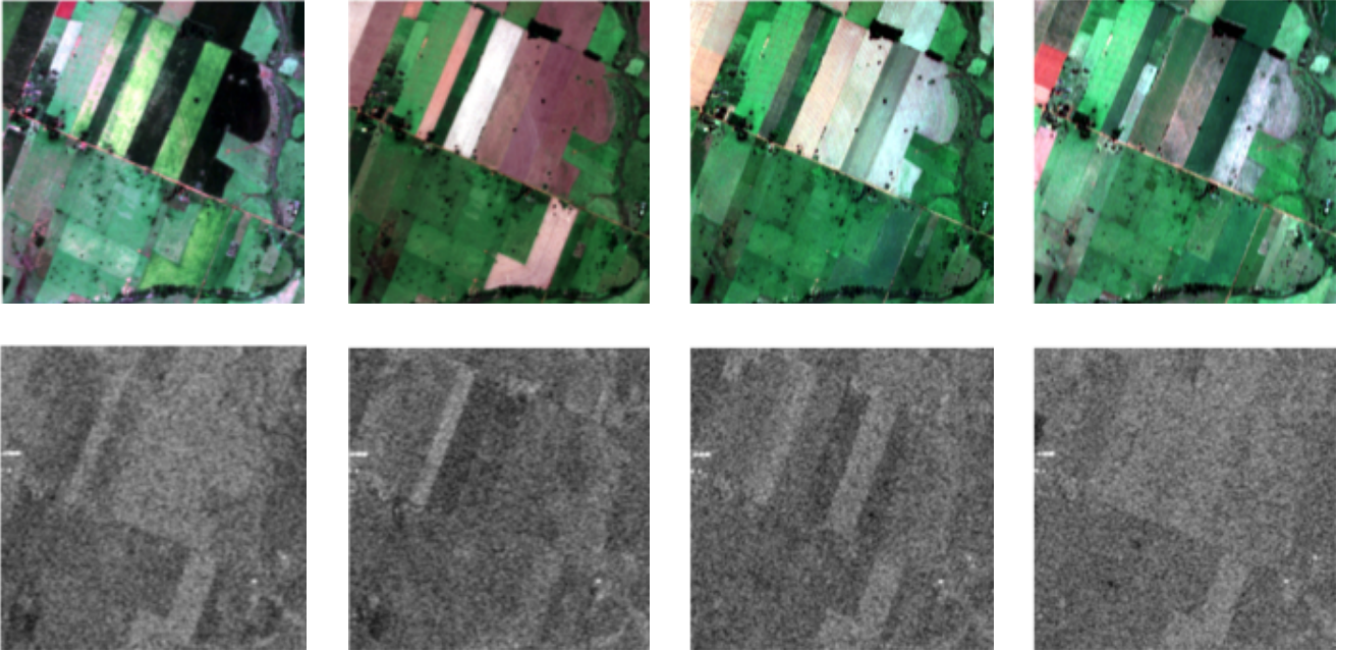


Fig. 7: Dataset sample: Sentinel-2 acquisitions (top row), Sentinel-1 acquisitions (bottom row)

training-validation split that should ensure a balance of ROIs.

The dataset was divided into training and validation datasets by minimising the dissimilarity between the cumulative histograms computed on several random splits. The algorithm used is shown in Algorithm 1. For each random split, 90% for the training dataset and 10% for the validation dataset, N images from both the datasets are used to compute respectively the training cumulative histogram and the validation cumulative histogram. Then the dissimilarity between these two histograms is computed by the equation 1 and it is saved in the vector \vec{d} .

$$d = \frac{\frac{1}{N} \sum_{i=0}^N \left| \frac{h_{train}}{\#bins} - \frac{h_{val}}{\#bins} \right|}{\frac{1}{N} \sum_{i=0}^N \frac{h_{train}}{\#bins}} \quad (1)$$

By selecting the minimum of the vector \vec{d} , the algorithm returns the training and validation split with the lower value of dissimilarity, or in other words the split that ensure a certain level of similarity between training and validation datasets.

Algorithm 1: Training-Validation split

```

for  $i \leftarrow 1$ , number of splits do
   $train_i, val_i \leftarrow$  random split dataset (90%-10%);
   $train\_s \leftarrow$  select  $N$  samples of  $train_i$ ;
   $val\_s \leftarrow$  select  $N$  samples of  $val_i$ ;
   $train\_hist \leftarrow$  cumulative histogram of  $train\_s$ ;
   $val\_hist \leftarrow$  cumulative histogram of  $val\_s$ ;
   $\vec{d}_i \leftarrow$  dissimilarity( $train\_hist, val\_hist$ );
end
 $best\_split \leftarrow argmin \vec{d}_i$ ;
return  $train_{best\_split}, val_{best\_split}$ ;

```

For the experiments done in this paper, the number of splits tested was 2000, with N equals to 150 and number of bins equal to 20.

C. Images registration

Although the data downloaded from the Google Earth Engine platform are geo-referenced, there may be co-registration errors, often evident in time series. In fact for Sentinel-2 data, as shown in Table I, in the 1% of cases the co-registration error can be higher than 1.5 pixels [34]. On the other hand, for Sentinel-1 GRD (Ground Range Detected) products, the error should always be below < 0.25 pixels [35].

Co-registration error	$0 < X < 0.5$ pixels	$0.5 < X < 1$ pixels	$1 < X < 1.5$ pixels	$X > 1.5$ pixels
S2A % of products	58%	35%	6%	1%
S2B % of products	47%	41%	11%	1%

TABLE I: Multi-temporal performance statistics for Sentinel 2 constellation [34].

While convolutional networks can handle small co-registration errors, as we will show below, we have modified the model's evaluation metrics to compensate for such errors.

D. Evaluation metrics

Let $\hat{\mathbf{Y}} \in \mathbb{R}^{W \times H \times B}$ be a reference image (i.e. ground truth) such that: $\hat{\mathbf{Y}} = [\hat{\mathbf{y}}_1, \dots, \hat{\mathbf{y}}_H] = [\hat{\mathbf{y}}^1, \dots, \hat{\mathbf{y}}^N]$, where $\hat{\mathbf{y}}_k \in \mathbb{R}^{1 \times N}$ ($k \in \{1, \dots, H\}$) is the k^{th} band of $\hat{\mathbf{Y}}$ and $\hat{\mathbf{y}}^i \in \mathbb{R}^{H \times 1}$ ($i \in \{1, \dots, N\}$) is the i^{th} pixel of $\hat{\mathbf{Y}}$. Let $\mathbf{Y} \in \mathbb{R}^{W \times H \times B}$ be the predicted image. The quality measures used in this work to evaluate the fusion results are the following:

- 1) **PSNR:** *PSNR* (Peak Signal-to-Noise Ratio) measures the quality of the spatial reconstruction of each hyper-spectral band. *PSNR* is the ratio between the maximum

power of the k^{th} band of the reference image and the residual error between the k^{th} bands of the reference and of the estimated images. For the k^{th} band, *PSNR* is computed as follows:

$$PSNR(\hat{\mathbf{y}}_k, \mathbf{y}_k) = 10 \log_{10} \left(\frac{\max(\hat{\mathbf{y}}_k)^2}{\|\hat{\mathbf{y}}_k - \mathbf{y}_k\|_2^2 / N} \right), \quad (2)$$

where $\max(\hat{\mathbf{y}}_k)$ is the maximum pixel value of the k^{th} band for the reference image $\hat{\mathbf{Y}}$. The residual error is normalized for each band and thus it is not affected by data values which allows fair comparison between the bands. The final value of *PSNR* is the average of the *PSNR* value of each band. An high value of *PSNR* indicates that the reconstruction is of high quality.

- 2) **SSIM**: The Structural Similarity Index Measure (*SSIM*) measures the similarity between two images $\hat{\mathbf{Y}}$ and \mathbf{Y} . The comparison is performed on the basis of luminance, contrast and structure of the images as follows:

$$SSIM(\hat{\mathbf{Y}}, \mathbf{Y}) = \frac{(2\mu_{\hat{\mathbf{Y}}}\mu_{\mathbf{Y}} + C_1)(2\sigma_{\hat{\mathbf{Y}}\mathbf{Y}} + C_2)}{(\mu_{\hat{\mathbf{Y}}}^2 + \mu_{\mathbf{Y}}^2 + C_1)(\sigma_{\hat{\mathbf{Y}}}^2 + \sigma_{\mathbf{Y}}^2 + C_2)}, \quad (3)$$

where C_1 and C_2 are constants, $\mu_{\hat{\mathbf{Y}}}$, $\mu_{\mathbf{Y}}$, $\sigma_{\hat{\mathbf{Y}}}$ and $\sigma_{\mathbf{Y}}$ are respectively the means and the standard deviations of the real and of the generated images and $\sigma_{\hat{\mathbf{Y}}\mathbf{Y}}$ is defined as follows:

$$\sigma_{\hat{\mathbf{Y}}\mathbf{Y}} = \frac{1}{N-1} \sum_{j=1}^N (\hat{\mathbf{Y}}_j - \mu_{\hat{\mathbf{Y}}})(\mathbf{Y}_j - \mu_{\mathbf{Y}}). \quad (4)$$

SSIM computes values between 0 and 1, where 1 means "very similar" and 0 "very different".

- 3) **FID**: The Frechet Inception Distance (*FID*) compares the distribution of generated images with the distribution of real images estimating the quality based on how well the model Inception v3 classifies the images. Since the results given by this metric depend on a neural network, it is possible to choose if the model used has to be pre-trained or not. In this case the model uses a random initialisation without pre-trained weights. *FID* is calculated taken the 2048 activations from the last pooling layer of the Inception v3 model: the real image $\hat{\mathbf{Y}}$ and the generated image \mathbf{Y} are each one predicted as 2048 activation features and then are used in the calculation as follows:

$$FID = \|\mu_{\hat{\mathbf{Y}}} - \mu_{\mathbf{Y}}\|^2 + Tr(C_{\hat{\mathbf{Y}}} + C_{\mathbf{Y}} - 2\sqrt{C_{\hat{\mathbf{Y}}}C_{\mathbf{Y}}}), \quad (5)$$

where $\mu_{\hat{\mathbf{Y}}}$, $\mu_{\mathbf{Y}}$, $C_{\hat{\mathbf{Y}}}$ and $C_{\mathbf{Y}}$ are the means and the covariances for the real and the generated images, respectively, and *Tr* is the trace linear algebra operation (i.e. the sum of the elements along the main diagonal of the square matrix). Lower scores indicate the two groups of images are more similar, or have more similar statistics. The perfect score is 0 that indicates the two groups of images are identical.

- 4) **SAM**: *SAM* (Spectral Angle Mapper) [36] measures the quality of the spectral reconstruction by computing the angle between two spectral vectors at each pixel in

the reference and in the reconstructed image. For two spectral vectors, $\hat{\mathbf{y}}^i$ and \mathbf{y}^i , *SAM* is measured as follows:

$$SAM = \arccos \left(\frac{\langle \hat{\mathbf{y}}^i, \mathbf{y}^i \rangle}{\|\hat{\mathbf{y}}^i\|_2 \|\mathbf{y}^i\|_2} \right). \quad (6)$$

The values of *SAM* are measured in degrees: the smaller the absolute value of *SAM*, the weaker the spectral distortion and the higher the spectral quality of the fusion (the ideal value is 0). The final *SAM* value is computed by averaging all the *SAMs* of the pixels of the image.

- 5) **MSE and RMSE**: *MSE* (Mean-Squared Error) is simply the mean squared error between the original image $\hat{\mathbf{Y}}$ and its estimation \mathbf{Y} as follows:

$$MSE(\hat{\mathbf{Y}}, \mathbf{Y}) = \frac{\sum_{j=1}^N (\hat{\mathbf{Y}}_j - \mathbf{Y}_j)^2}{N}. \quad (7)$$

RMSE (Root-Mean-Square Error) is its squared root and measures the L^2 error between the original image $\hat{\mathbf{Y}}$ and its estimation \mathbf{Y} as follows:

$$RMSE(\hat{\mathbf{Y}}, \mathbf{Y}) = \frac{\|\mathbf{Y} - \hat{\mathbf{Y}}\|_F}{\sqrt{N \times H}}, \quad (8)$$

where $\|\hat{\mathbf{Y}}\|_F = \sqrt{\text{trace}(\hat{\mathbf{Y}}^T \hat{\mathbf{Y}})}$ is the Frobenius norm of $\hat{\mathbf{Y}}$. The ideal value for *MSE* and *RMSE* is 0.

- 6) **CC**: Cross Correlation (*CC*) is defined as follows:

$$CC(\hat{\mathbf{Y}}, \mathbf{Y}) = \frac{1}{H} \sum_{k=1}^H CCS(\hat{\mathbf{y}}_k, \mathbf{y}_k), \quad (9)$$

where *CCS* is the cross correlation between two single-banded images, \mathbf{A} and \mathbf{B} , and it is defined as follows:

$$CCS(\mathbf{A}, \mathbf{B}) = \frac{\sum_{j=1}^N (\mathbf{A}_j - \mu_A)(\mathbf{B}_j - \mu_B)}{\sqrt{\sum_{j=1}^N (\mathbf{A}_j - \mu_A)^2 \sum_{j=1}^N (\mathbf{B}_j - \mu_B)^2}}, \quad (10)$$

where $\mu_A = \frac{1}{N} \sum_{j=1}^N \mathbf{A}_j$ is the mean of \mathbf{A} , μ_B is the mean of \mathbf{B} and N is the number of the pixels. The ideal value of *CC* is 1.

- 7) **DD**: The measure of Degree of Distortion (*DD*) between two images $\hat{\mathbf{Y}}$ and \mathbf{Y} is defined as follows:

$$DD(\hat{\mathbf{Y}}, \mathbf{Y}) = \frac{1}{N \times H} \|\text{vec}(\hat{\mathbf{Y}}) - \text{vec}(\mathbf{Y})\|_1,$$

where N is the number of the pixels, H is the number of the bands and $\text{vec}(\hat{\mathbf{Y}})$ and $\text{vec}(\mathbf{Y})$ represent the vectorization of the images $\hat{\mathbf{Y}}$ and \mathbf{Y} , respectively. The ideal value of *DD* is 0.

- 8) **Q or UQI**: The Universal image Quality Index (*Q* or *UQI*) was suggested by Wang and Bovik [37] to evaluate the similarity between two single-band images. It measures their distortion as the product of loss of correlation, luminance distortion and contrast distortion. The *Q* index between two single-band images \mathbf{A} and \mathbf{B} is defined as follows:

$$Q(\mathbf{A}, \mathbf{B}) = \frac{4\sigma_{AB}^2 \mu_A \mu_B}{(\sigma_A^2 + \sigma_B^2)(\mu_A^2 + \mu_B^2)} \quad (11)$$

where μ_A, μ_B, σ_A^2 and σ_B^2 are the means and the variances of \mathbf{A} and \mathbf{B} , respectively, and σ_{AB} is the covariance of (\mathbf{A}, \mathbf{B}) . The range of Q is $[-1, 1]$ and its ideal value is 1.

The Co-registration Shift Compensation (CSC) has been developed and applied to all the metrics in order to incorporate the co-registration error suppression in the metrics. The suppression method consists of dividing an image into sub-images, and for each sub-image the metric is calculated by offsetting the ground truth with respect to the prediction by one or more pixels. By averaging all the results, the final metric is obtained.

E. Experimental Results

This section will present the qualitative and quantitative results calculated on the outputs produced by applying the models to the validation dataset. In particular, three examples are reported with qualitative and quantitative results:

a) *Test 1*: Figure 8 and Table II.

	Ground Truth	LSTM	GAN	Combined
PNSR	inf	29.02	30.15	28.92
SSIM	1.0	0.94	0.91	0.95
FID	0.0	140.49	239.80	160.69
CSC-PSNR (x1000)	0.0	1.25	0.97	1.28
RMSE	0.0	0.04	0.03	0.04
SAM	0.0	0.09	0.09	0.09
UQI	1.0	0.99	0.99	0.99
DD	0.0	0.03	0.02	0.03
CC	1.0	0.94	0.94	0.95

TABLE II: Models score - Test 1 (Fig. 8)

b) *Test 2*: Figure 9 and Table III

	Ground Truth	LSTM	GAN	Combined
PNSR	inf	16.47	27.10	25.03
SSIM	1.0	0.59	0.87	0.86
FID	0.0	493.84	175.72	250.49
CSC-PSNR (x1000)	0.0	22.56	1.95	3.14
RMSE	0.0	0.15	0.04	0.06
SAM	0.0	0.48	0.18	0.21
UQI	1.0	0.79	0.97	0.95
DD	0.0	0.12	0.03	0.04
CC	1.0	0.35	0.93	0.92

TABLE III: Models score - Test 2 (Fig. 9)

c) *Test 3*: Figure 10 and Table IV

In order to give more statistical value to the experimental results, we computed the metrics on 100 random samples from the dataset. In Table V are reported the averaged metrics for the LSTM, the GAN and the combiner model. The Table V demonstrated our expectation: the combiner models performed better than the other two, since it is able to concentrate the best features captured by the GAN and the LSTM.

	Ground Truth	LSTM	GAN	Combined
PNSR	inf	28.48	27.07	27.67
SSIM	1.0	0.91	0.78	0.88
FID	0.0	78.15	133.89	84.28
CSC-PSNR (x1000)	0.0	1.42	1.96	1.71
RMSE	0.0	0.04	0.04	0.04
SAM	0.0	0.12	0.13	0.11
UQI	1.0	0.98	0.99	0.98
DD	0.0	0.03	0.03	0.03
CC	1.0	0.82	0.75	0.83

TABLE IV: Models score - Test 3 (Fig. 10)

	Ground Truth	LSTM	GAN	Combined
PNSR	inf	24.23	25.04	27.06
SSIM	1.0	0.87	0.80	0.88
FID	0.0	199.01	336.03	224.75
CSC-PSNR (x1000)	0.0	5.98	14.90	3.54
RMSE	0.0	0.07	0.09	0.05
SAM	0.0	0.16	0.18	0.13
UQI	1.0	0.92	0.90	0.93
DD	0.0	0.06	0.07	0.04
CC	1.0	0.71	0.52	0.83

TABLE V: Models average scores on 100 samples

IV. CONCLUSIONS

In this manuscript a novel method for clouds removal has been presented. The main novelties are: 1) the use of a joint data fusion paradigm combining the spatio-temporal features extracted by an LSTM and a GAN; 2) the use of time-series of data, rarely explored in the state of the art for this peculiar objective. Quantitative and qualitative results have shown a good ability of image regeneration both in terms of low level of noise and details preservation. Future developments will include exploring the proposed method with more complex datasets (e.g. multispectral, multipolarimetric, longer time series, etc.) and optimizing the parameters and structure of the overall proposed method.

ACKNOWLEDGMENTS

The research work published in this manuscript has been developed in collaboration with the European Space Agency (ESA) Φ -lab during the traineeship of Maria Pia Del Rosso and Alessandro Sebastianelli in the period July-October 2019 and the traineeship of Erika Puglisi in the period February-October 2020. This research is also supported by the ongoing Open Space Innovation Platform (OSIP) project titled "AI powered cross-modal adaptation techniques applied to Sentinel-1 and -2 data" under a joint collaboration between the European Space Agency (ESA) Φ -Lab and the University of Sannio.

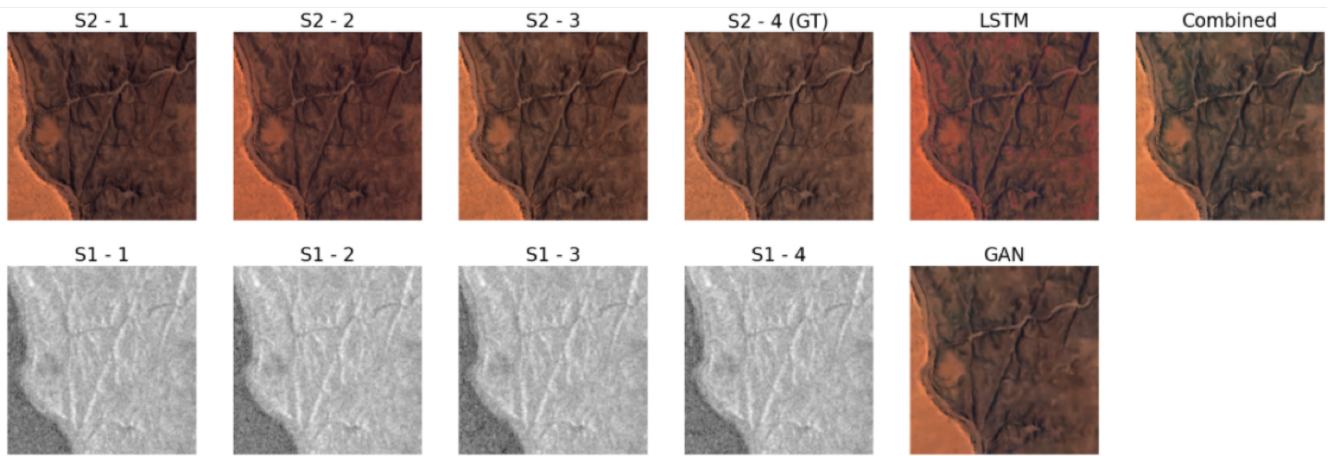


Fig. 8: Test 1

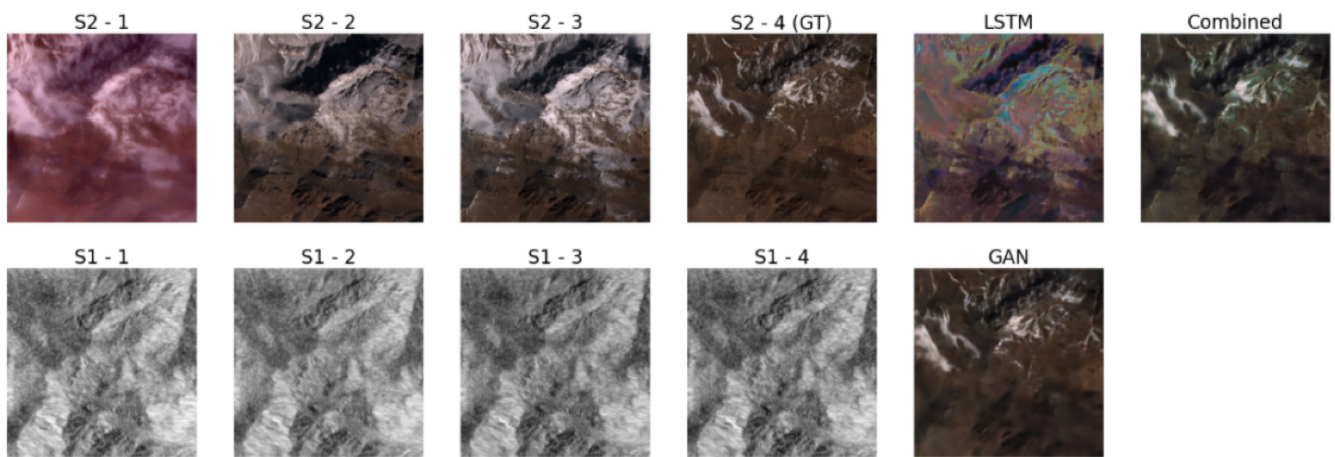


Fig. 9: Test 2

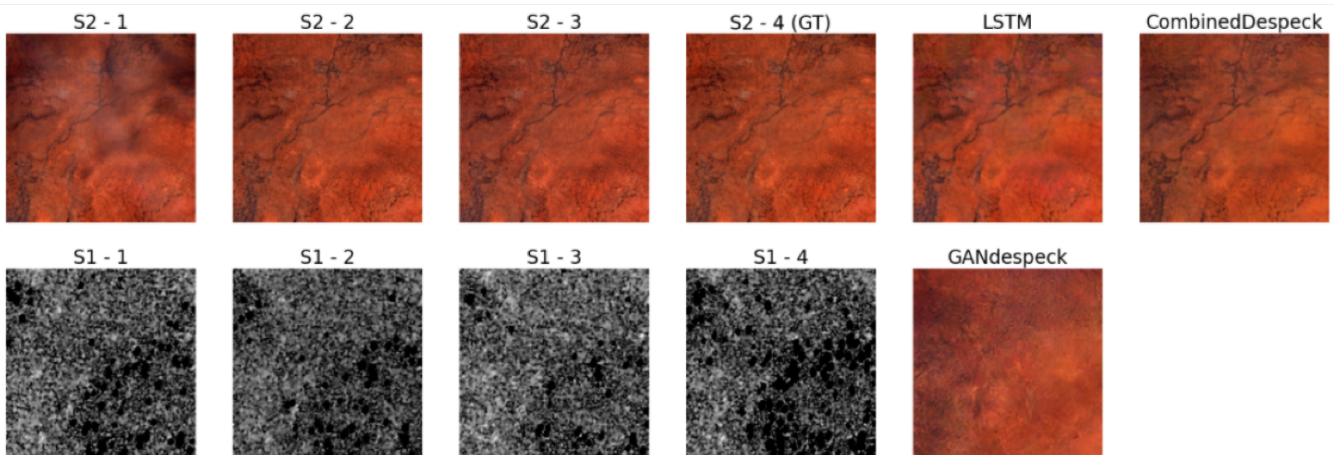


Fig. 10: Test 3

REFERENCES

- [1] NASA Earth Observation (NAO), "Cloud Fraction (1 mont - Acqua/Modis)," https://neo.sci.gsfc.nasa.gov/view.php?datasetId=MYDAL2_M_CLD_FR&year=2020.
- [2] G. Hu, X. Li, and D. Liang, "Thin cloud removal from remote sensing images using multidirectional dual tree complex wavelet transform and transfer least square support vector regression," *Journal of Applied Remote Sensing*, vol. 9, no. 1, p. 095053, 2015.
- [3] M. Xu, X. Jia, M. Pickering, and S. Jia, "Thin cloud removal from optical remote sensing images using the noise-adjusted principal components transform," *ISPRS Journal of Photogrammetry and Remote Sensing*, vol. 149, pp. 215–225, 2019.
- [4] Z. Zhu and C. E. Woodcock, "Continuous change detection and classification of land cover using all available landsat data," *Remote sensing of Environment*, vol. 144, pp. 152–171, 2014.

- [5] M. Xu, M. Pickering, A. J. Plaza, and X. Jia, "Thin cloud removal based on signal transmission principles and spectral mixture analysis," *IEEE Transactions on Geoscience and Remote Sensing*, vol. 54, no. 3, pp. 1659–1669, 2015.
- [6] T. Wang, J. Shi, H. Letu, Y. Ma, X. Li, and Y. Zheng, "Detection and removal of clouds and associated shadows in satellite imagery based on simulated radiance fields," *Journal of Geophysical Research: Atmospheres*, vol. 124, no. 13, pp. 7207–7225, 2019.
- [7] H. Lv, Y. Wang, and Y. Shen, "An empirical and radiative transfer model based algorithm to remove thin clouds in visible bands," *Remote Sensing of Environment*, vol. 179, pp. 183–195, 2016.
- [8] H. Choi and R. Bindschadler, "Cloud detection in landsat imagery of ice sheets using shadow matching technique and automatic normalized difference snow index threshold value decision," *Remote Sensing of Environment*, vol. 91, no. 2, pp. 237–242, 2004.
- [9] C.-H. Lin, P.-H. Tsai, K.-H. Lai, and J.-Y. Chen, "Cloud removal from multitemporal satellite images using information cloning," *IEEE transactions on geoscience and remote sensing*, vol. 51, no. 1, pp. 232–241, 2012.
- [10] F. Ramoimo, F. Tutunaru, F. Pera, and O. Arino, "Ten-meter sentinel-2a cloud-free composite—southern africa 2016," *Remote Sensing*, vol. 9, no. 7, p. 652, 2017.
- [11] X. Li, H. Shen, L. Zhang, and H. Li, "Sparse-based reconstruction of missing information in remote sensing images from spectral/temporal complementary information," *ISPRS journal of photogrammetry and remote sensing*, vol. 106, pp. 1–15, 2015.
- [12] X. Li, L. Wang, Q. Cheng, P. Wu, W. Gan, and L. Fang, "Cloud removal in remote sensing images using nonnegative matrix factorization and error correction," *ISPRS journal of photogrammetry and remote sensing*, vol. 148, pp. 103–113, 2019.
- [13] R. Eckardt, C. Berger, C. Thiel, and C. Schmullius, "Removal of optically thick clouds from multi-spectral satellite images using multi-frequency sar data," *Remote Sensing*, vol. 5, no. 6, pp. 2973–3006, 2013.
- [14] F. Meng, X. Yang, C. Zhou, and Z. Li, "A sparse dictionary learning-based adaptive patch inpainting method for thick clouds removal from high-spatial resolution remote sensing imagery," *Sensors*, vol. 17, no. 9, p. 2130, 2017.
- [15] Q. Zhang, Q. Yuan, C. Zeng, X. Li, and Y. Wei, "Missing data reconstruction in remote sensing image with a unified spatial-temporal-spectral deep convolutional neural network," *IEEE Transactions on Geoscience and Remote Sensing*, vol. 56, no. 8, pp. 4274–4288, 2018.
- [16] Q. Zhang, Q. Yuan, J. Li, Z. Li, H. Shen, and L. Zhang, "Thick cloud and cloud shadow removal in multitemporal imagery using progressively spatio-temporal patch group deep learning," *ISPRS Journal of Photogrammetry and Remote Sensing*, vol. 162, pp. 148–160, 2020.
- [17] I. J. Goodfellow, J. Pouget-Abadie, M. Mirza, B. Xu, D. Warde-Farley, S. Ozair, A. Courville, and Y. Bengio, "Generative adversarial networks," *arXiv preprint arXiv:1406.2661*, 2014.
- [18] P. Ebel, A. Meraner, M. Schmitt, and X. X. Zhu, "Multisensor data fusion for cloud removal in global and all-season sentinel-2 imagery," *IEEE Transactions on Geoscience and Remote Sensing*, pp. 1–13, 2020.
- [19] M. Mirza and S. Osindero, "Conditional generative adversarial nets," *arXiv preprint arXiv:1411.1784*, 2014.
- [20] C. Grohnfeldt, M. Schmitt, and X. Zhu, "A conditional generative adversarial network to fuse sar and multispectral optical data for cloud removal from sentinel-2 images," in *IGARSS 2018-2018 IEEE International Geoscience and Remote Sensing Symposium*. IEEE, 2018, pp. 1726–1729.
- [21] A. Meraner, P. Ebel, X. X. Zhu, and M. Schmitt, "Cloud removal in sentinel-2 imagery using a deep residual neural network and sar-optical data fusion," *ISPRS Journal of Photogrammetry and Remote Sensing*, vol. 166, pp. 333–346, 2020.
- [22] V. Sarukkai, A. Jain, B. Uzcent, and S. Ermon, "Cloud removal from satellite images using spatiotemporal generator networks," in *Proceedings of the IEEE/CVF Winter Conference on Applications of Computer Vision*, 2020, pp. 1796–1805.
- [23] S. Oehmcke, T.-H. K. Chen, A. V. Prishchepov, and F. Gieseke, "Creating cloud-free satellite imagery from image time series with deep learning," in *Proceedings of the 9th ACM SIGSPATIAL International Workshop on Analytics for Big Geospatial Data*, 2020, pp. 1–10.
- [24] H. Pan, "Cloud removal for remote sensing imagery via spatial attention generative adversarial network," *arXiv preprint arXiv:2009.13015*, 2020.
- [25] P. Singh and N. Komodakis, "Cloud-gan: Cloud removal for sentinel-2 imagery using a cyclic consistent generative adversarial networks," in *IGARSS 2018-2018 IEEE International Geoscience and Remote Sensing Symposium*. IEEE, 2018, pp. 1772–1775.
- [26] W. He and N. Yokoya, "Multi-temporal sentinel-1 and-2 data fusion for optical image simulation," *ISPRS International Journal of Geo-Information*, vol. 7, no. 10, p. 389, 2018.
- [27] J. Gao, Q. Yuan, J. Li, H. Zhang, and X. Su, "Cloud removal with fusion of high resolution optical and sar images using generative adversarial networks," *Remote Sensing*, vol. 12, no. 1, p. 191, 2020.
- [28] F. N. Darbaghshahi, M. R. Mohammadi, and M. Soryani, "Cloud removal in remote sensing images using generative adversarial networks and sar-to-optical image translation," *arXiv preprint arXiv:2012.12180*, 2020.
- [29] A. Sebastianelli, M. P. Del Rosso, P. P. Mathieu, and S. L. Ullo, "Paradigm selection for data fusion of sar and multispectral sentinel data applied to land-cover classification," *arXiv preprint. Submitted to IEEE Geoscience and Remote Sensing Letters*, 2021.
- [30] O. Ronneberger, P. Fischer, and T. Brox, "U-net," *MICCAI2015*, 2015.
- [31] Z. Zhou, M. M. Rahman Siddiquee, N. Tajbakhsh, and J. Liang, "Unet++: A nested u-net architecture for medical image segmentation," in *Lecture Notes in Computer Science (including subseries Lecture Notes in Artificial Intelligence and Lecture Notes in Bioinformatics)*, 2018.
- [32] Z. Zhou, M. M. R. Siddiquee, N. Tajbakhsh, and J. Liang, "UNet++: Redesigning Skip Connections to Exploit Multiscale Features in Image Segmentation," *IEEE Transactions on Medical Imaging*, 2020.
- [33] Sebastianelli Alessandro, Del Rosso Maria Pia and Ullo Silvia, "Automatic Dataset Builder for Machine Learning Applications to Satellite Imagery." [Online]. Available: <https://arxiv.org/abs/2008.01578>
- [34] European Space Agency, "Sentinel-2 11c data quality report," <https://sentinels.copernicus.eu/web/sentinel/user-guides/sentinel-2-msi/document-library>, online; accessed 15 March 2021.
- [35] —, "Sentinel-1 product definition," <https://sentinel.esa.int/documents/247904/1877131/Sentinel-1-Product-Definition>, online; accessed 15 March 2021.
- [36] F. A. Kruse, A. Lefkoff, J. Boardman, K. Heidebrecht, A. Shapiro, P. Barloon, and A. Goetz, "The spectral image processing system (sips)—interactive visualization and analysis of imaging spectrometer data," *Remote sensing of environment*, vol. 44, no. 2-3, pp. 145–163, 1993.
- [37] Z. Wang and A. C. Bovik, "A universal image quality index," *IEEE signal processing letters*, vol. 9, no. 3, pp. 81–84, 2002.